Physica C: Superconductivity and its applications 601 (2022) 1354111

Contents lists available at ScienceDirect

Physica C: Superconductivity and its applications

journal homepage: www.elsevier.com/locate/physc

Probing effect of strain field on Ca diffusion in $BaZrO_3$-doped $YBa_2Cu_3O_{7-x}$ /$Ca_{0.3}Y_{0.7}Ba_2Cu_3O_{7-x}$ multilayer nanocomposite films

Victor Ogunjimi [a,*], Mohan Panth [a], Mary Ann Sebastian [b,c], Di Zhang [d], Timothy Haugan [b], Haiyan Wang [d], Judy Wu [a]

[a] Department of Physics and Astronomy, the University of Kansas, Lawrence, Kansas 66045, USA
[b] U.S Air Force Research Laboratory, Aerospace Systems Directorate, WPAFB, OH 45433, USA
[c] University of Dayton Research Institute, Dayton, OH 45469, USA
[d] School of Materials Engineering, Purdue University, West Lafayette, IN 47907, USA

ARTICLE INFO

Keywords:
YBCO nanocomposites
1D artificial pinning center
Vortex pinning efficiency
Coherent interface
Interficial strain
Dynamic lattice enlargement

ABSTRACT

Recently, we reported that incorporating thin $Ca_{0.3}Y_{0.7}Ba_2Cu_3O_{7-x}$ spacer layers in $BaZrO_3$/ $YBa_2Cu_3O_{7-x}$ (BZO/YBCO) films in multilayers (ML) could lead to a coherent BZO/YBCO interface due to reduced lattice mismatch of ~1.4% and hence improved pinning by the BZO 1D artificial pinning centers (BZO 1D-APCs). It was hypothesized that the highly strained YBCO columns around the BZO 1D-APCs due to the larger lattice constant of BZO than YBCO's in c-axis by 7.7% provide channels to facilitate Ca diffusion more preferably near the BZO/YBCO interface, leading to an enlarged YBCO's c-axis lattice constant as a consequence of the Ca/Cu substitution on the YBCO's Cu-O planes. Confirmation of this hypothesis is hence important to understand the mechanism of Ca diffusion in BZO/YBCO ML films for further enhancement of pinning efficiency of the BZO 1D-APCs. Motivated by this, this work presents a comparative study of two sets of BZO/YBCO ML films: singly-doped (SD-ML, BZO only) and the doubly-doped (DD-ML, BZO + Y_2O_3). The modulated strain field in the SD-ML films is in contrast to the non-modulated strain in the DD-ML samples as confirmed by transmission electron microscopy. Interestingly, improved pinning by >four times of the reference SD single-layer (SD-SL) film' was observed in the SD-ML samples even when the constituent BZO/YBCO layer thickness was varied between 50-100 nm, indicating that the Ca diffusion along the strained BZO/YBCO interface and the Ca/Cu substitution on YBCO's Cu-O planes indeed correlate with the modulated strain field. In contrast, pinning degrades by >twice in DD-ML samples with respect to their DD-SL counterpart's. This result therefore suggests that strained BZO/YBCO interfaces serve as channels for Ca diffusion in SD-ML, which leads to the coherent BZO/YBCO interfaces and hence improved pinning of BZO 1D-APCs. This effect diminishes when such a modulated strain field is removed in the DD-ML samples.

1. Introduction

Artificial pinning centers (APCs) self-organized in $REBa_2Cu_3O_{7-x}$ (REBCO, RE-rare earth elements Y, Gd, Sm, etc.) films have been utilized to demobilize quantized magnetic vortices and hence provide improved superconducting current-carry capacity. C-axis aligned nanorods of insulating impurities, such as $BaZrO_3$ (BZO) [1–5], $BaHfO_3$ (BHO) [6–10], $BaSnO_3$ [11,12] $YBa_2(Nb/Ta)O_6$ [13,14] etc, have been shown to be effective one-dimensional (1D) APCs for magnetic vortices oriented along the c-axis. The pinning effectiveness of these impurity 1D-APCs is strongly affected by the APC/REBCO interface and a sharp insulator/superconductor interface is critical to achieve optimal pinning since pinning force that is proportional to the radial derivative of the pinning energy across the BZO/YBCO interface [15]. However, the microstructure of the BZO 1D-APC/YBCO interface has been reported to be defective due to the large BZO/YBCO lattice mismatch of ~ 7.7%, which leads to less sharp BZO 1D-APC/YBCO interface [16–18]. The strained 1D-APC/YBCO interface has also been reported in other 1D-APC/YBCO nanocomposites due to the similar reason of large APC/YBCO lattice mismatch including BHO/YBCO at 6.9%, BSO/YBCO

* Corresponding author at: Physics and Astronomy, University of Kansas College of Liberal Arts and Sciences, 1251 Wescoe Hall Dr. Lawrence, Kansas 66045, United States.
E-mail addresses: victorogunjimi@ku.edu (V. Ogunjimi), jwu@ku.edu (J. Wu).

https://doi.org/10.1016/j.physc.2022.1354111
Received 8 February 2022; Received in revised form 22 June 2022; Accepted 23 July 2022
Available online 4 August 2022

at 5.7% and $YBa_2(Nb/Ta)O_6$/YBCO at 2.9%. This defective interface may vary in different APC/REBCO nanocomposites and may explain a large range of the pinning force density (F_p) reported for different kinds of 1D-APCs. For example, a higher $F_p > 180$ GN/m^3 was reported for BHO 1D-APCs at 65 K in contrast to ~ 70 GN/m^3, 103 GN/m^3 [9] and 122 GN/m^3 [13] respectively, for BZO, BSO and $YBa_2(Nb/Ta)O_6$ 1D-APCs. Since APC/YBCO interfacial strain is the driving force for the self-assembly of 1D-APCs [18,19], selection of APC materials with no or very small lattice mismatch with YBCO may not be an option to achieve 1D-APCs with high concentration and desired morphology and dimension.

In a recent work to probe the effect of the BZO 1D-APC/YBCO interface on pinning, we explored a multilayer (ML) approach by inserting two thin $Ca_{0.3}Y_{0.7}Ba_2Cu_3O_{7-x}$ (CaY-123) spacers into the BZO/YBCO nanocomposite films to facilitate Ca diffusion from the spacers to BZO/YBCO during or immediately after the BZO 1D-APC formation [20,21]. The hypothesis was that the tensile strained YBCO columns of a few nm in thickness around the BZO 1D-APCs serve as effective diffusion channels for a Ca ion, which is about 30% larger than Cu ion and Ca/Cu substitution is hence energetically favorable on tensile strained YBCO lattice. A high resolution scanning transmission electron microscopy (HRSTEM) and elemental mapping study has confirmed Ca/Cu substitution on the Cu-O planes of YBCO through formation of short segmented planar defects or stacking faults in the YBCO columns. This leads to elongation of c-axis parameter from 1.17 nm in undoped YBCO to about 1.26 nm [20] in the YBCO columns around the BZO 1D-APCs in the BZO/YBCO ML films, resulting in much reduced BZO/YBCO lattice mismatch to ~ 1.4% and a highly coherent BZO/YBCO interface. Consequently, as much as five-fold enhancement of critical current density J_c at B//c-axis was reported and the enhanced F_p ~158 GN/m^3 at 65 K indicates the pinning efficiency of BZO 1D-APCs is indeed affected sensitively by the BZO/YBCO interface [21].

While the ML approach has shown a promising result in modifying the BZO/YBCO interface, its mechanism is barely understood. Specifically, the hypothesis of the Ca/Cu substitution facilitated by the strong tensile strain near the BZO/YBCO interface needs further investigation. In this work, an additional Y_2O_3 APC is introduced to the BZO/YBCO ML nanocomposites to modify the strain field, especially to reduce or eliminate the modulated strain field by the c-axis aligned BZO 1D-APCs. As shown in the experiment on the BZO+Y_2O_3 doped YBCO nanocomposite films [22] and the simulation based on an elastic strain energy model [23], Y_2O_3 typically form nanoparticles (NPs) in YBCO due to its negative lattice mismatch (smaller lattice constant than YBCO's) with YBCO and hence can modify local strain field and the nucleation and evolution of the BZO 1D-APCs. Consequently, the well-modulated strain field, especially the Ca-diffusion channels of tensile strained YBCO columns around the BZO 1D-APCs, in BZO singly-doped YBCO (SD-ML) would no longer be the case in the BZO+Y_2O_3 doubly-doped YBCO (DD-ML) samples. By comparing the pinning efficiency of the BZO 1D-APCs in the SD-ML and DD-ML YBCO films, we aim to shed lights on the mechanism of Ca diffusion.

2. Experimental

A set of 6 vol.% BZO doped YBCO (SD) and another of 6 vol.% BZO + 3 vol.% Y_2O_3 doped YBCO (DD) were fabricated using pulsed laser deposition (PLD) [4,9,24] on (100) $SrTiO_3$ (STO) single crystal substrates. Each set comprised of both single-layer (SL) and multi-layer (ML) films. The two SL films, denoted as SD-SL and DD-SL, are ~ 150 nm thick and serve as the references. All ML films have two 10 nm-thick CaY-123 spacers (layer number N = 2) and 3 layers of either BZO/YBCO or (BZO+Y_2O_3)/YBCO (layer number M = 3) as shown in Table 1. There are two ML films in the SD set. Each BZO/YBCO layer of the SD-ML150 (SD-ML300) are 50 nm (100 nm) thick. The DD set has only one ML film, denoted as DD-ML, having each of its three (BZO+Y_2O_3)/YBCO layers with a thickness of 50 nm. All ML samples have a structure of YBCO/CaY-123/YBCO/CaY-123/YBCO/substrates except the YBCO layer either SD or DD. For all samples, the substrate temperature was 825 °C and the partial pressure of oxygen was 300 mTorr during the PLD. After the PLD deposition, the samples were annealed in one atmosphere O_2 pressure at 500 °C for 30 minutes. The PLD repetition rates were 2 Hz and 8 Hz for the deposition of the CaY-123 spacers and doped YBCO layers respectively. The SL samples have the thickness ~ 150 nm and were used as the reference for comparison with the ML samples.

Transmission electron microscopy (TEM) were taken using a Thermo Fisher Scientific TALOS F200X TEM system with a point-to-point resolution of 1.6 Å. A Bruker D8 Discover diffractometer was used to generate X-ray diffraction (XRD) θ-2θ patterns. These measurements were acquired using X-rays Cu-kα radiation of wavelength 1.54 Å. The XRD peak intensities of each film was normalized to the YBCO (005) peak. A shadow mask was used to sputter Ag contacts on the films for electrical transport measurement. The c-axis length is derived only from the YBCO (005) peak. There are several reasons for this. The first reason is due to peak overlap of the YBCO (00l) peaks with substrate peaks and dopant peaks. As seen in the 2θ-ω scans, the YBCO (005) peak is one of the few peaks without overlap. For example, YBCO (003) peak and the STO (001) peak overlap, as well as the YBCO (006) and STO (002) peaks. Secondly, broadening of the peaks can occur at higher 2θ. Thirdly, the YBCO (001) peak has a small intensity. For all of these reasons, given the composition of our film and the substrate and dopants utilized, the YBCO (005) peak was chosen to calculate the c-lattice constant.

Diffraction peaks were identified using the Bruker EVA software analysis with references of PDF 00-035-0734 for SrTiO3 (STO substrate), PDF 00-038-1433 for YBCO, PDF 00-055-1002 for BaZrO3 (BZO), 01-087-0956 for (Y0.9 Ca0.10)$Ba_2Cu_3O_{6.92}$, and PDF 00-043-0661 for Y_2O_3. The EVA analysis lists the identified peaks, with an identification caption that is related to the peak intensity, the 2θ angle associated with the peak, and the d-spacing. From Bragg's law: $\lambda = 2d_{hkl}\sin\theta$, where λ is the x-ray wavelength, θ is the angle at which a family of planes produces a diffraction peak, and d is the space between the planes. Since YBCO has an orthorhombic structure, the relationship $1/d^2 = h^2/a^2 + k^2/b^2 + l^2/c^2$ exists. Peaks for analysis were chosen where h=k=0, which occurs for the (005) peak of YBCO. The equation then simplifies to c = SQRT(l^2d^2), where c is the c-lattice parameter [25].

Standard photolithography was used to pattern two 500 μm long bridges with width 20 μm and 40 μm respectively. The thickness and

Table 1
Summary of the some of the important parameters such as c-lattice constant, FWHM of the YBCO (005) Rocking curve (RC), critical temperature(T_c), $F_{p,max}$ (at 65K) and B_{max} (at 65K) Of the SD-SL, SD-ML150, SD-ML300, DD-SL and DD-ML films. M represents the number of BZO/YBCO (or BZO + Y2O3)/YBCO) layer and N represents the number of Ca doped layer.

Sample ID	Sample structure	C-lattice parameter (Å)	(005) RC FWHM	Tc (K)	Fpmax at 65K (GNm^{-3})	Bmax at 65K (GNm^{-3})
SD-SL	M = 1, N =0	11.82	0.59°	86.5	39.7	7.0
SD-ML150	M = 3, N = 2	11.76	0.38°	84.5	157.7	8.0
SD-ML300	M = 3, N = 2	11.73	0.32°	83.5	122.8	8.0
DD-SL	M = 1, N = 0	11.74	0.88°	87.8	67.5	7.0
DD-ML	M = 3, N = 2	11.72	0.51°	86.0	28.5	5.0

lateral dimension of the bridges were determined using a Tencor P-16 profilometer. The current-voltage (*I-V*) data were acquired at temperatures (65K-77K) in a Quantum Design Ever-Cool II Physical Property Measurement system (PPMS) with magnetic field (***B***) up to 9.0 T. Critical current density (J_c) was measured using a 1 μV/cm standard criterion [5,6,26]. The *N* value is proportional to the pinning potential barrier energy of the BZO 1D- APCs and it can be obtained through fitting the measured *I-V* curves using the formula of $V \propto I^N$ [27]. The *N* values were calculated at minimum voltages in the range of ~0.01 μV – 0.1 μV and maximum voltages of a few μV.

3. Results and discussions

A schematic illustrating the microstructures of SD-ML (Fig. 1a) and DD-ML (Fig. 1b) shows the difference in the strain field in the two cases. In the SD-ML sample, modulated strain field with the maximum tensile strain expected at the BZO 1D-APC/YBCO interface (white YBCO column around the 1D-APC) decreases monotonically with the distance from the interface in the direction perpendicular to the 1D-APC. Considering the c-axis aligned BZO 1D-APCs extend through the films thickness, the highly strained YBCO columns may serve as effective channels facilitating diffusion of Ca from the CaY-123 spacers to the SD-ML films [28]. The extension of the BZO 1D-APCs through the thickness of a SD-SL film is confirmed in TEM image shown in Fig. 1c. In the DD-ML sample (Fig. 1b), the modulated strain field may no longer be present due to the modification of the local strain field by the Y_2O_3 NPs. Consequently, the BZO APCs are mostly shown as short segments with a large spread of orientations or NPs (denoted by circles) as confirmed in TEM results shown in Fig. 1d. This may impact Ca diffusion directly due to the lack of diffusion channels formed along the BZO 1D-APC/YBCO interface as in the case of SD-ML in Fig. 1a. In addition, the strong tensile strain near the BZO/YBCO interface would be much reduced, which means that the Ca/Cu substitution may no longer be energetically favorable over Ca/Y and Ca/Ba substitutions in DD-ML samples if Ca diffusion occurs across the interface of CaY-123 spacers and doped YBCO layers.

Fig. 2a compares the XRD θ-2θ spectra of SD-ML300 (red), SD-ML150 (blue), DD-SL (purple), DD-ML (green) and SD-SL (black) films. Clearly, the results show epitaxial grown films in the *c*-direction on (100) STO substrate as evidenced by the *(00l)* YBCO peaks. The presence of Y_2O_3 NPs in the DD films is confirmed by the Y_2O_3 (222) peak at ~ 30°. It should be noted that the peaks associated to impurities of BZO and Y_2O_3 have fairly low intensities due to the small amount of impurity doping. However, they could be clearly identified as detailed in our earlier reports [21,29] and in Fig.s S1 – S5 (Supplemental Information) depicts the original XRD spectrum taken on SD-SL, SD-ML150, SD-ML300, DD-SL and DD-ML respectively (see Table 1) with all identified peaks including those that can only be indexed to BZO listed in Table S1 – S5 (Supplemental Information). The *c*-lattice constant of 11.82 Å for the SD-SL film is the largest among the samples studied in this work (Table 1). This is consistent to the reported values in literature due to the high tensile strain on the YBCO lattice as a result of doping of BZO which

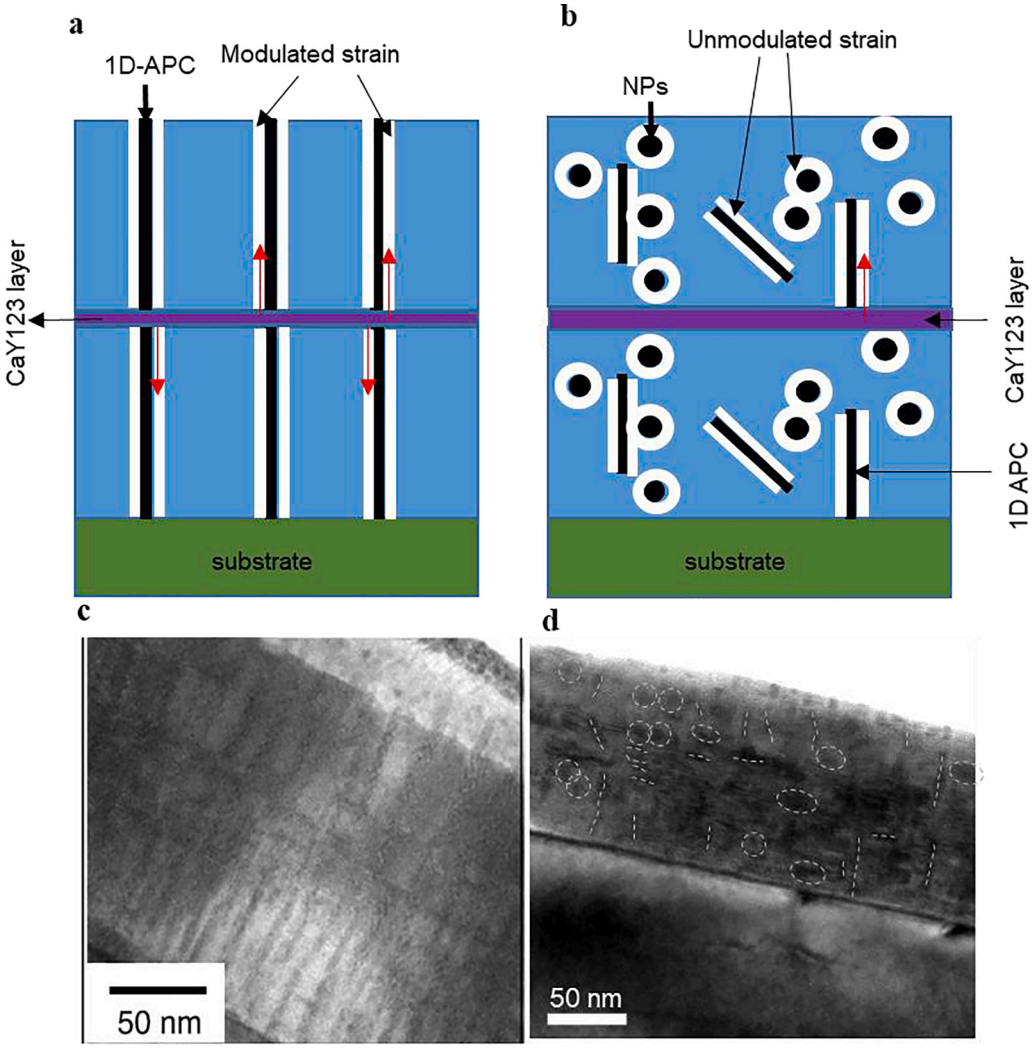

Fig. 1. Schematic description of microstructures of: (a) SD-ML film with modulated strain (white regions) due to the large lattice mismatch at the 1D-APC/YBCO interface, and (b) unmodulated strain around segmented 1D-APCs and NPs. The red arrow depicts the diffusion of Ca from the CaY-123 spacer layer. TEM cross-sectional images of (c) the SD-SL with only BZO 1D-APCs aligned in the c-axis of YBCO and (d) DD-SL samples with both segmented BZO 1D-APCs and NPs of BZO or/and Y_2O_3 NPs (marked with dashed lines).

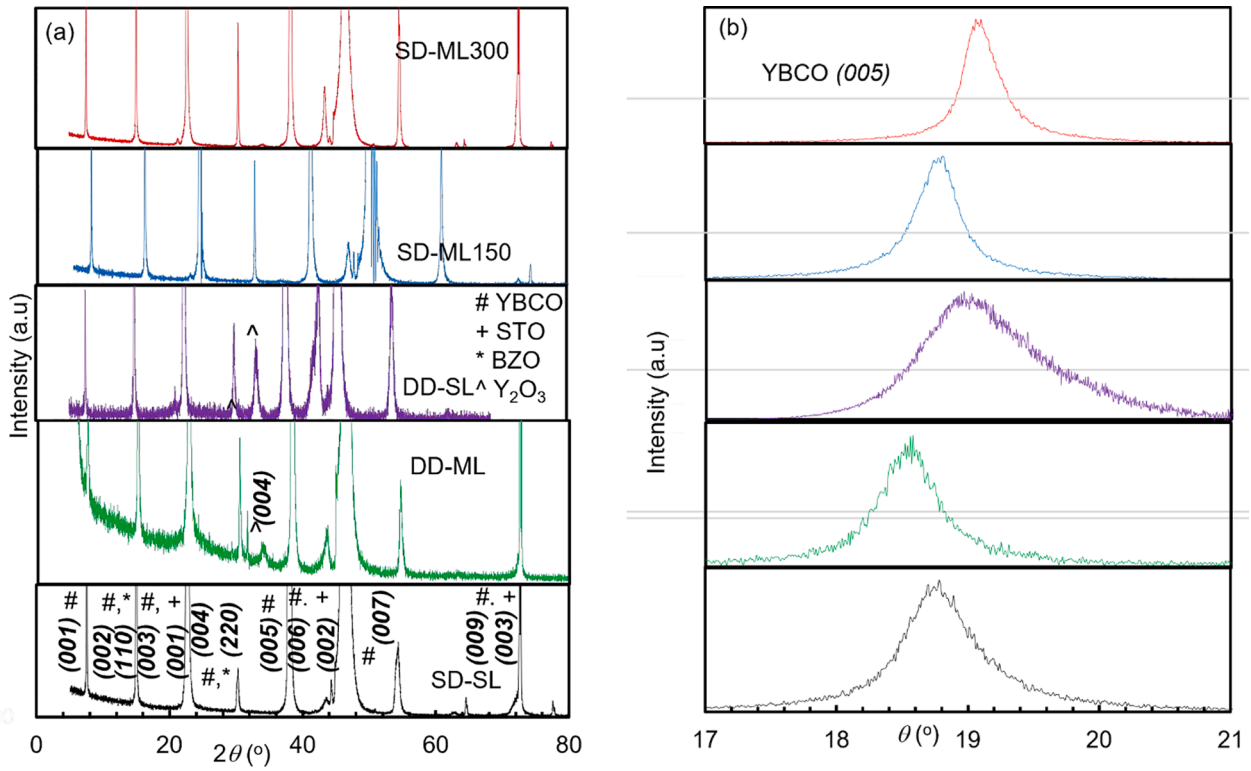

Fig. 2. X-ray diffraction scans. (a) θ -2θ-scans taken on SD-SL (black), DD-SL (purple), DD-ML (green), SD-ML150 (blue) and SD-ML300 (red) samples respectively. The spectra were generated using Cu-kα radiation of wavelength 1.54 Å. The symbols #, +, * and ˆ represent the YBCO, STO substrate, major BZO and Y_2O_3 peaks respectively. (b) Rocking curves of the YBCO (005) peak for the same five films.

has a larger lattice constant [30,31]. The c-axis lattice constants are considerably reduced to 11.76 Å and 11.73 Å for the SD-ML150 and SD-ML300 samples respectively, which are considerably smaller than that of ~12.6 Å measured using TEM [20,21]. The difference may be attributed to the different sample scale under the two measurements. In the former, the c-lattice constant is an average over a large area under the x-ray beam, typically on the order of several millimeter in dimension. In the latter, it represents the local c-lattice constant over a small area of a few to a few tens of nanometer in TEM study. It should be noted that the enlarged YBCO c-axis lattice constant occurs only locally near the BZO 1DAPC/YBCO interfaces due to formation of planer defects or stacking faults induced by Ca/Cu replacement on Cu-O planes as revealed in the TEM study [20,21]. This means the c-lattice constant is not uniform in BZO/YBCO nanocomposite films as reported previously [20,21,32,33]. Interestingly, the c-axis lattice constants of 11.72 Å and 11.75 Å for the DD-SL and DD-ML respectively are comparable to that of the SD-ML150 and SD-ML300. In the DD-SL case, the presence of Y_2O_3 NPs is known to cause misalignment and segmentation of the BZO 1D-APCs as discussed earlier in Fig.s 1b and 1d. The reduced c-axis lattice constant in DD-SL as compared to the SD-SL's is therefore anticipated from the local strain modification and the BZO APC morphology and orientation change by Y_2O_3 NPs. A similar case is expected in DD-ML case since the first CaY-123 spacer was deposited on a 50 nm thick DD-SL layer (the first of the three BZO+Y_2O_3/YBCO layers in the DD-ML samples) and would not affect the microstructure of this layer and would allow extension of the microstructure to upper BZO+Y_2O_3/YBCO layers due to the small thickness of 10 nm for CaY-123 spacers [20,21]. Fig. 2b compares the XRD rocking curves of the YBCO (005) peaks of the same five films. The peak locations for all five samples fall within ~ 18.4° to ~ 19.2°. The full width at half maximum (FWHM) of the YBCO (005) rocking curves are 0.59°, 0.38° and 0.32° for the SD-SL, SD-ML150 and SD-ML300 respectively (Table 1), indicating a reduction in microstrain due to Ca doping in the two SD-ML samples as compared to their SD-SL counterpart's. The similar trend of YBCO's (005) FWHM reduction was also observed earlier in 2 vol.% BZO/YBCO ML samples and was attributed to a better nanocomposite microstructure as a consequence of the coherent BZO 1D-APC/YBCO interface and much more straightened and better aligned BZO 1D-APCs [20]. This is certainly not the case in DD samples. As shown in Table 1, the YBCO's (005) FWHMs for the two DD samples of DD-SL and DD-ML samples are 0.88° and 0.51° respectively. They are significantly larger than that for the two SD-ML samples. In fact, the large FWHMs of the DD samples are not surprising since they are expected from the truncated and misaligned BZO 1D-APCs in these samples, which lead the crystal lattice distortion on YBCO. Interestingly, the FWHM is moderately reduced in the DD-ML sample as compared to the DD-SL's. Since the former has a lower T_c of 86.0 K, as opposed to 87.8 K for the latter, the reduced FWHM is likely associated to the Ca diffusion into the BZO+Y_2O_3/YBCO layers in the DD-ML sample via other pathways. Figs. 3a and 3b respectively compare the $J_c(B)$ and pinning force density $\boldsymbol{F_p}$ (B) curves (where $\boldsymbol{F_p} = \boldsymbol{J_c} \times \boldsymbol{B}$) at 65 K (to minimize T_c effect) in magnetic field $\boldsymbol{B}$//c-axis of the SD-SL (black, T_c ~ 86.5 K), SD-ML150 (blue, T_c ~ 84.5 K), DD-SL (green, T_c ~ 87.8 K) and DD-ML (purple, T_c ~ 86.0 K) films. Overall, the DD films have higher T_c values (See Table 1) relative to that of the SD films. This may be attributed to reduced strain field overlap due to the presence of Y_2O_3 NPs [5]. Two main observations are evident in these graphs. First, the comparison of the SD-ML (blue) and DD-ML (purple) films shows that the former has the lower J_c susceptibility to B and therefore much higher F_p. Quantitatively, the J_c values are 2.3 MA/cm^2 and 0.9 MA/cm^2 for the SD-ML and DD-ML respectively at 2.0 T. When the field is increased to 9.0 T the J_c for the SD-ML is still as high as ~1.7 MA/cm^2 while the J_c measured in the DD-ML decreases to as low as ~ 0.2 MA/cm^2. The corresponding $F_p(B)$ data (Fig. 3b) confirms the relative strong pinning in the SD-ML film as reflected in both high values and low J_c susceptibility to B as observed in Fig. 3a. As expected, the SD-ML sample exhibit overall higher F_p values in the entire range of the

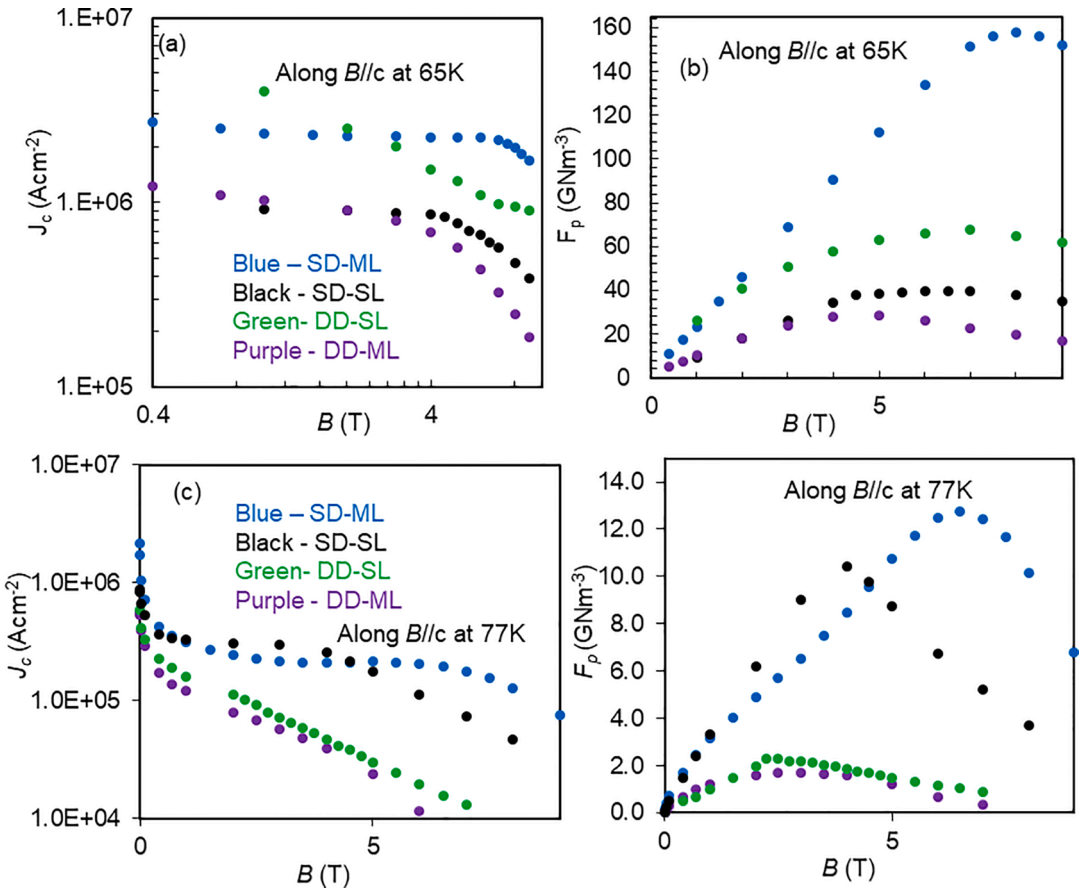

Fig. 3. The pinning properties of J_c (B) and $F_{p,max}$ (B) measured at $B//c$ on SD-SL (black), DD-ML (purple), DD-SL (green), SD-ML150 (blue) at 65 K (a and b) and at 77 K (c and d), respectively.

magnetic field. The value of the $F_p(B)$ peak (F_{pmax}) and the location of the F_{pmax} (B_{max}) differ considerably. A clear contrast in magnitude is clearly seen with $F_{p,max}$ of ~ 158 GNm^{-3} at 8.0 T and ~ < 28.5 GNm^{-3} at 5.0 T for the SD-ML film and DD-ML respectively. Since the enhanced pinning efficiency of the BZO 1D-APCs is attributed to their coherent interface with YBCO enabled by YBCO's c-lattice constant elongation due to Ca diffusion and the follow-up Ca/Cu substitution on YBCO's Cu-O planes [20,21], the not as-good pinning in DD-ML case indicates that such a mechanism of Ca diffusion is no longer the case.

Secondly, the comparison between the DD-SL (green) and DD-ML (purple) films indicates that while J_c susceptibility at fields < ~ 4.0 T is higher in the former, the overall J_c in the latter is much lower. At 5.0 T and 9.0 T, for example, the J_c values in the latter are ~ 2.7 and ~ 2.0 times lower respectively than in the former. Similarly, a much higher $F_{p,max}$ of ~ 67.5 GNm^{-3} in the DD-SL is ~2.4 times of the $F_{p,max}$ ~ 28.5 GNm^{-3} in the DD-ML (Fig. 3b). The corresponding 77 K data are shown in Figs. 3c-3d and similar $J_c(B)$ and F_p (B) trends are seen here as seen at 65 K. Interestingly, the SD-ML sample has the highest overall F_p (B) among the four samples in comparison, despite its T_c ~84.5 K is the lowest among the four samples. This again indicates the difference in the Ca diffusion mechanism in the SD-ML and DD-ML samples. In particular, the modulated tensile strain field in the former seems to be essential to facilitating the Ca diffusion and Ca/Cu substitution at the BZO/YBCO interface for improved interface and hence pinning efficiency of the BZO 1D-APCs. This is certainly not the case when this modulated tensile strain field is reduced or removed in the DD-ML case. In fact, the $J_c(B)$ and F_p (B) are the worst in the DD-ML sample among the four in comparison. If the DD-ML and DD-SL have similar microstructures in terms of BZO and Y_2O_3 APCs, the lower $J_c(B)$ and F_p (B) in the former may be associated to the effect caused by Ca diffusion via other pathways. This argument is supported by the lower T_c ~86.0 K in DD-ML, which is 1.8 K lower than that of DD-SL (Table 1). This result therefore suggests that multiple pathways may be present for Ca diffusion from CaY-123 spacers to doped YBCO layers while the one facilitated by the modulated tensile strain near the BZO/YBCO interface is the only one demonstrating improved pinning so far.

In order to further probe the Ca diffusion mechanism facilitated by the modulated tensile strain field, Fig. 4 compares the $J_c(B)$ and F_p (B) curves of the two SD-ML samples with fixed CaY-123 thickness of t_{spacer} =10 nm and varying BZO/YBCO layer thickness of 50 nm (SD-ML150, blue) and 100 nm (SD-ML300, red) respectively. The SD-SL data (black) is also included as a reference. Interestingly, a comparable but slightly lower enhancement in J_c and F_p has been observed in SD-ML300 as compared to the SD-ML150 while both ML-SD films display strong pinning enhancement relative to the SD-SL film. At 2.0 T, the J_c enhancement factors of 2.6 and 2.0 can be observed for the SD-ML150 (blue) and SD-ML300 (red) respectively. The enhancement factors increase monotonically with increasing B field. At B=9.0 T, the J_c enhancements of 4.3 and 3.4 times respectively are observed for the SD-ML150 and SD-ML300 (Fig. 3a). The B_{max} values of both films are improved to 8.0 T (relative to the B_{max} of 6.0 T for the SD-SL) with F_{pmax} values of 158 GNm^{-3} and 122 GNm^{-3} for the SD-ML150 and SD-ML300 respectively. This result confirms the improved pinning efficiency of BZO 1D-APCs in the SD-ML150 case, in which Ca diffusion length is up to 50 nm [28], may be extended to SD-ML300 case where the Ca diffusion length is doubled.

Fig. 5a compares the N values as function of B of SD-SL(black), SD-ML150 (blue), SD-ML-300 (red) and DD-ML (purple) samples at $B//c$ and 65 K. For better visibility, Fig. 5b plots the N values for the three ML samples normalized to that for the SD-SL. Notably, the two SD-ML films

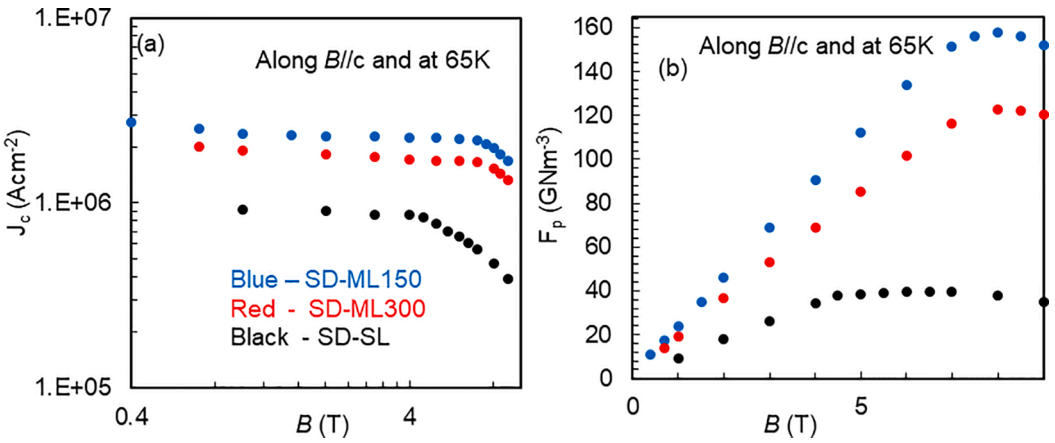

Fig. 4. J_c vs. B (a) and F_p vs B (b) curves measured with respect to varying Ca diffusion length at fixed CaY123 thickness, t_{spacer} =10 nm along θ =0° (B//c-axis) at 65K.

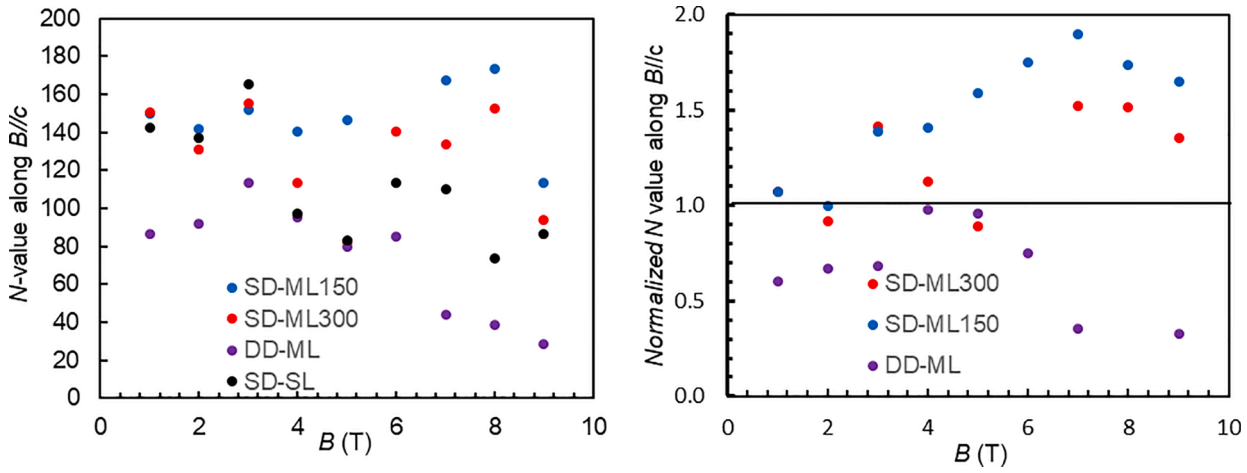

Fig. 5. N-values of the four 6% doped BZO/YBCO films calculated at 65K and B//c plotted as a function of B with (a) the raw N values and (b) the N value of the 3 ML films normalized to that of the SD-SL film.

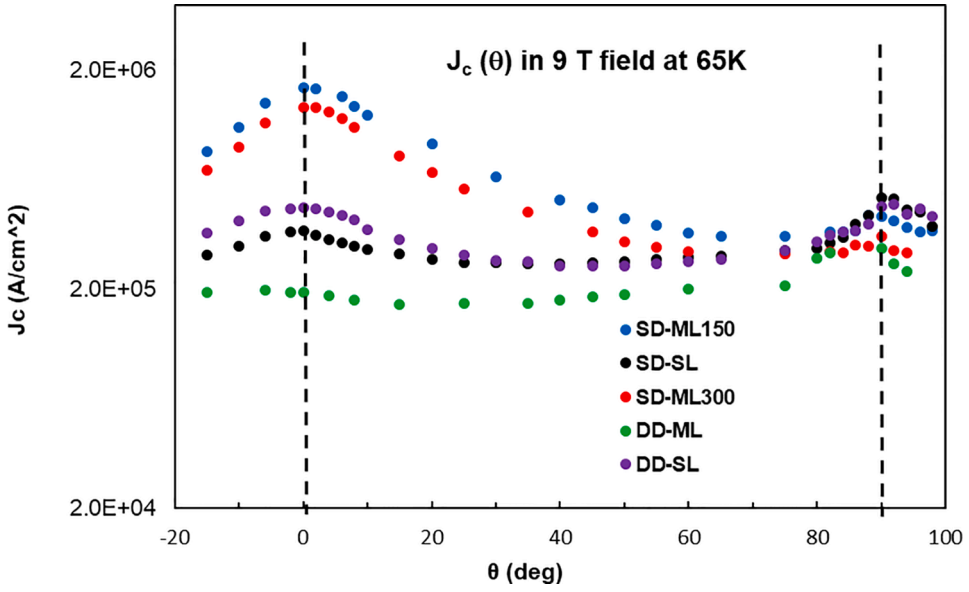

Fig. 6. Jc (θ) curves measured at 65 K in 9 T on SD-SL (black), SD-ML150 (blue), SD-ML300 (red), DD-SL (purple) and DD-ML (green).

have the highest N values indicating relatively strong pinning as confirmed in Figs. 3 and 4. The range of N values are ~ 94 – 155 and ~ 114 – 173 for the SD-ML300 and SD-ML150 respectively. In contrast, the DD-ML has overall lowest N value that is ~ 28 at 9.0 T. In most of the B field range the normalized N values are greater than one in the SD-ML films (black and red) confirming improved pinning potential of the BZO 1D-APCs in these films. It is interesting to note that the normalized N value data peaked near the B_{max} in all films.

The J_c (θ) curves measured at 65 K and 9.0 T are compared in Fig. 6 for the SD-SL, SD-ML150 and SD-ML300, DD-SL and DD-ML samples. Overall, the J_c (θ) curves for the DD films (green and purple) illustrate smaller variation while θ was varied from B//c-axis (θ=0) *to* B//ab-plane (θ=90°), which means a more isotropic pinning landscape associated to the mixed APC morphologies. The J_c anisotropy, defined as ($J_{c,\ max} - J_{c,\ min}$)/$J_{c,\ min}$, is ~ 96% and ~ 76% for the DD-SL and DD-ML respectively. This indicates that the DD-ML sample is the least anisotropic of the two DD films confirming that the isotropic benefit of the inclusion of NPs is not hindered in the ML structure. Nevertheless, the overall lower J_c (θ), especially the disappearance of the J_c peak at B//c-axis for the DD-ML sample is far from ideal and requires further investigation. In contrast, the two SD-ML samples both have much enhanced J_c (θ) values over a wide range of θ up to ~ 70-80°, at a trade-off of slightly reduced J_c (θ) at around B//ab-plane. The least isotropic landscape is seen in the SD-ML samples due to the strong improved pinning along B//c. The J_c anisotropy is 350% and 370% for the SD-ML150 and SD-ML300 respectively. The strong J_c enhancement along B//c at 9 T in the SD-ML films is evident in their high J_c ($\theta = 0^o$) peaks in contrast to the much smaller corresponding peak of the SD-SL sample.

From this comparative study of the microstructure and superconducting properties of SD-ML and DD-ML BZO/YBCO nanocomposite samples, several important insights have been obtained. First, the highly modulated strain field due to vertically aligned BZO 1D-APCs in BZO/YBCO SD-ML samples may provide effective channels for Ca ions to diffuse into the BZO 1D-APCs/YBCO interface. This allows Ca (30% larger than Cu)/Cu substitution on the Cu-O planes of YBCO since it is energetically favorable on tensile strained YBCO columns near the BZO 1D-APCs/YBCO interface. The consequent c-axis elongation of YBCO leads to reduced lattice mismatch with BZO at the BZO 1D-APCs/YBCO interface and hence improvement of the crystallinity of the BZO/YBCO nanocomposite film as indicated by the reduction of the YBCO (005) FWHMs, more straightened BZO 1D-APCs and coherent BZO 1D-APCs/YBCO interface. On the other hand, the destruction of such a modulated strain field in BZO+Y_2O_3/YBCO DD samples would demolish the Ca diffusion channels into the BZO 1D-APCs/YBCO interface. Nevertheless, other pathways of Ca diffusion from CaY-123 spacers into BZO/YBCO nanocomposites are present in both SD-ML and DD-ML samples as indicated in the reduced T_c values by 1-2 K in both SD-ML and DD-ML samples as compared to that of their counterparts without Ca doping, which is anticipated from the Ca-doping of YBCO. This Ca-doping induced T_c reduction may affect the J_c values at temperatures close to T_c, which may explain the overall lower J_c (B, θ) in DD-ML sample as compared to their DD-SL counterpart's. However, the improved BZO 1D-APCs/YBCO interface crystallinity in the SD-ML samples is shown to correlate to the enhanced pinning efficiency of the BZO 1D-APCs directly not only at ~B//c-axis (or B parallel to the 1D-APCs), but also in an extended angular range of B field orientation exceeding 60 degrees away from the c-axis.

4. Conclusion

In summary, a comparative study of microstructure and superconducting properties was carried out on singly-doped BZO/YBCO and doubly-doped BZO + Y_2O_3/YBCO nanocomposite ML films with two Ca-containing CaY-123 spacer layers of 10 nm each in thickness. The motivation is to probe the role of the modulated strain field in facilitating Ca diffusion in the former due to formation of c-axis aligned BZO 1D-APCs through the film thickness of YBCO with a large lattice mismatch. In contrast, such a modulated strain field is more or less destructed or diminished in the latter since the BZO 1D-APCs become short and misaligned segments in presence of the Y_2O_3 NPs. It has been found that the modulated strain field with the highest tensile strain initiated from the BZO 1D-APCs/YBCO interface due to the large lattice mismatch of ~7.7%, which decreases monotonically to the minimum at the middle point between two nearest-neighbor BZO 1D-APCs, provide effective channels for Ca ions to diffusion from CaY-123 spacers to YBCO near the BZO 1D-APCs/YBCO interface, leading to energetically favorable substation of smaller Cu by larger (by 30%) Ca ions on the Cu-O planes of YBCO. When such a modulated strain field is removed in the DD-ML samples, the Ca diffusion channels along the BZO 1D-APCs/YBCO interface are no longer present. Nevertheless, other channels of Ca diffusion may be present in both SD-ML and DD-ML samples, which has been confirmed in the comparable T_c reduction of 1-2 K in both of them as compared to their SL counterparts'. It should be noted that the effect of Ca diffusion facilitated by the modulated strain field near the BZO 1D-APCs/YBCO interface differs fundamentally from that through the other channels. The former leads to improved crystallinity of the BZO 1D-APCs/YBCO interface due to elongation of the YBCO's c-lattice constant as Cu in the Cu-O planes is partially replaced with Ca, which leads to significantly enhanced pinning efficiency of BZO 1D-APCs. At 65 K and 9.0 T, the $F_{p,max}$ at B//c-axis exhibits an enhancement by a factor of 3-4 in SD-ML samples as compared to their SD-SL counterparts'. In contrast, when this mechanism is removed in the DD-ML samples, no enhancement of pinning was observed. Furthermore, the T_c reduction resulted from the other Ca diffusion mechanisms may be responsible for reduced J_c and pinning in DD-ML samples as compared to their DD-SL counterparts', suggesting general Ca doping in YBCO may not be favorable to enhancing vortex pinning.

Author statement

None.

Declaration of Competing Interest

The authors declare that they have no known competing financial interests or personal relationships that could have appeared to influence the work reported in this paper.

Acknowledgments

This research was supported in part by NSF contracts Nos: NSF-DMR-1909292 and NSF-ECCS-1809293, the AFRL Aerospace Systems Directorate, the Air Force Office of Scientific Research (AFOSR) LRIR #14RQO8COR and LRIR #18RQCOR100. D.Z. and H.W. acknowledge the support from the U.S. National Science Foundation for the high resolution STEM effort at Purdue University (DMR-1565822 and DMR-2016453).

Supplementary materials

Supplementary material associated with this article can be found, in the online version, at doi:10.1016/j.physc.2022.1354111.

References

[1] J. MacManus-Driscoll, et al., Strongly enhanced current densities in superconducting coated conductors of YBa 2 Cu 3 O 7–x+ BaZrO 3, Nat. Mater. 3 (7) (2004) 439.
[2] K. Matsumoto, P. Mele, Artificial pinning center technology to enhance vortex pinning in YBCO coated conductors, Supercond. Sci. Technol. 23 (1) (2009), 014001.
[3] S.H. Wee, et al., Engineering nanocolumnar defect configurations for optimized vortex pinning in high temperature superconducting nanocomposite wires, Sci. Rep. (3) (2013) 2310.

[4] F.J. Baca, et al., Interactive growth effects of rare-earth nanoparticles on nanorod formation in YBa2Cu3Ox thin films, Adv. Funct. Mater. 23 (38) (2013) 4826–4831.
[5] S. Chen, et al., Enhancement of isotropic pinning force in YBCO films with BaZrO3 nanorods and Y2O3 nanoparticles, IEEE Trans. Appl. Supercond. 27 (4) (2017) 4–8.
[6] B. Gautam, et al., Microscopic adaptation of BaHfO3 and Y2O3 artificial pinning centers for strong and isotropic pinning landscape in YBa2Cu3O7–x thin films, Supercond. Sci. Technol. 31 (2) (2018), 025008.
[7] T. Matsushita, Flux pinning in superconducting 123 materials, Supercond. Sci. Technol. 13 (6) (2000) 730.
[8] S. Miura, et al., Characteristics of high-performance BaHfO3-doped SmBa2Cu3Oy superconducting films fabricated with a seed layer and low-temperature growth, Supercond. Sci. Technol. 28 (6) (2015), 065013.
[9] M.A.P. Sebastian, et al., Study of the flux pinning landscape of YBCO thin films with single and mixed phase additions BaMO3+ Z: M= Hf, Sn, Zr and Z= Y2O3, Y211, IEEE Trans. Appl. Supercond. 27 (4) (2017) 1–5.
[10] H. Tobita, et al., Fabrication of BaHfO3 doped Gd1Ba2Cu3O7− δ coated conductors with the high Ic of 85 A/cm-w under 3 T at liquid nitrogen temperature (77 K), Supercond. Sci. Technol. 25 (6) (2012), 062002.
[11] P. Mele, et al., Ultra-high flux pinning properties of BaMO3-doped YBa2Cu3O7− x thin films (M= Zr, Sn), Supercond. Sci. Technol. 21 (3) (2008), 032002.
[12] C. Varanasi, et al., Thick YBa 2 Cu 3 O 7− x+ BaSnO 3 films with enhanced critical current density at high magnetic fields, Appl. Phys. Lett. 93 (9) (2008), 092501.
[13] D. Feldmann, et al., Improved flux pinning in YBa2Cu3O7 with nanorods of the double perovskite Ba2YNbO6, Supercond. Sci. Technol. 23 (9) (2010), 095004.
[14] L. Opherden, et al., Large pinning forces and matching effects in YBa 2 Cu 3 O 7-δ thin films with Ba 2 Y (Nb/Ta) O 6 nano-precipitates, Sci. Rep. 6 (2016) 21188.
[15] G. Blatter, et al., Vortices in high-temperature superconductors, Rev. Mod. Phys. 66 (4) (1994) 1125–1388.
[16] S. Foltyn, et al., Materials science challenges for high-temperature superconducting wire, Nat. Mater. 6 (9) (2007) 631.
[17] B. Gautam, et al., Probing the effect of interface on vortex pinning efficiency of one-dimensional BaZrO3 and BaHfO3 artificial pinning centers in YBa2Cu3O7-x thin films, Appl. Phys. Lett. 113 (21) (2018), 212602.
[18] J. Wu, et al., Pinning efficiency of one-dimensional artificial pinning centers in YBa 2 Cu 3 O 7-x thin films, IEEE Trans. Appl. Supercond. 29 (5) (2019) 1–5.
[19] J.J. Shi, J.Z. Wu, Micromechanical model for self-organized secondary phase oxide nanorod arrays in epitaxial YBa2Cu3O7− δ films, Philos. Mag. 92 (23) (2012) 2911–2922.
[20] V. Ogunjimi, et al., Enhancing magnetic pinning by BaZrO3 nanorods forming coherent interface by strain-directed Ca-doping in YBa2Cu3O7− x nanocomposite films, Supercond. Sci. Technol. 34 (10) (2021), 104002.
[21] J.Z. Wu, et al., Enabling coherent BaZrO3 nanorods/YBa2Cu3O7-x interface through dynamic lattice enlargement in vertical epitaxy of BaZrO3/YBa2Cu3O7-x nanocomposites, Supercond. Sci. Technol. (2022).
[22] B. Gautam, et al., Towards isotropic vortex pinning in YBCO films with double-doping BHO-Y2O3 and BZO-Y2O3 artificial pining centers, in: IOP Conference Series: Materials Science and Engineering, IOP Publishing, 2017.
[23] J. Wu, J. Shi, Interactive modeling-synthesis-characterization approach towards controllable in situ self-assembly of artificial pinning centers in RE-123 films, Supercond. Sci. Technol. 30 (10) (2017), 103002.
[24] F. Baca, et al., Control of BaZrO 3 nanorod alignment in YBa 2 Cu 3 O 7− x thin films by microstructural modulation, Appl. Phys. Lett. 94 (10) (2009), 102512.
[25] B. Cullity, S. Stock, S. Stock, Elements of X-ray Diffraction, 3rd Ed., Prentice Hall, New Jersey, 2001.
[26] R. Emergo, et al., The effect of thickness and substrate tilt on the BZO splay and superconducting properties of YBa2Cu3O7− δ films, Supercond. Sci. Technol. 23 (11) (2010), 115010.
[27] L. Civale, et al., Identification of intrinsic ab-plane pinning in YBa/sub 2/Cu/sub 3/O/sub 7/thin films and coated conductors, IEEE Trans. Appl. Supercond. 15 (2) (2005) 2808–2811.
[28] V. Ogunjimi, et al., Enhancing magnetic pinning by BaZrO3 nanorods forming coherent interface by strain-directed Ca-doping in YBa2Cu3O7-x nanocomposite films. Superconductor Science and Technology, 2021.
[29] S. Chen, et al., Generating mixed morphology BaZrO3 artificial pinning centers for strong and isotropic pinning in BaZrO3–Y2O3 double-doped YBCO thin films, Superconduct. Sci. Technol. 30 (12) (2017), 125011.
[30] M.Z. Khan, et al., Enhanced flux pinning isotropy by tuned nanosized defect network in superconducting YBa 2 Cu 3 O 6+ x films, Sci. Rep. 9 (1) (2019) 1–12.
[31] S. Samoilenkov, et al., Anisotropic strain of BaZrO3, BaCeO3 and Y2O3 nanoinclusions in a YBa2Cu3O7− x epitaxial film matrix and its relation to the oxygen content of the superconductor, Supercond. Sci. Technol. 24 (5) (2011), 055003.
[32] C. Cantoni, et al., Strain-driven oxygen deficiency in self-assembled, nanostructured, composite oxide films, Acs Nano 5 (6) (2011) 4783–4789.
[33] T. Horide, et al., Structural evolution induced by interfacial lattice mismatch in self-organized YBa2Cu3O7− δ nanocomposite film, ACS Nano 11 (2) (2017) 1780–1788.